

Tunable Fragile Topology in Floquet Systems

Rui-Xing Zhang^{1,2,*} and Zhi-Cheng Yang^{2,3,†}

¹Condensed Matter Theory Center, Department of Physics,
University of Maryland, College Park, Maryland 20742-4111, USA

²Joint Quantum Institute, University of Maryland, College Park, MD 20742, USA

³Joint Center for Quantum Information and Computer Science,
University of Maryland, College Park, MD 20742, USA

We extend the notion of fragile topology to periodically-driven systems. We demonstrate driving-induced fragile topology in two different models, namely, the Floquet honeycomb model and the Floquet π -flux square-lattice model. In both cases, we discover a rich phase diagram that includes Floquet fragile topological phases protected by crystalline rotation or mirror symmetries, Floquet Chern insulators, and trivial atomic phases, with distinct boundary features. Remarkably, the transitions between different phases can be feasibly achieved by simply tuning the driving amplitudes, which is a unique feature of driving-enabled topological phenomena. Moreover, corner-localized fractional charges are identified as a “smoking-gun” signal of fragile topology in our systems. Our work paves the way for studying and realizing fragile topology in Floquet systems.

Introduction.— Topological band insulators usually differ from trivial insulators by the existence of anomalous gapless boundary modes, a manifestation of their non-trivial bulk topology [1, 2]. Various momentum-space topological invariants have been proposed to diagnose possible topology for a given set of energy bands, e.g. the Chern number [3] and the \mathbb{Z}_2 index [4] etc. It was recently realized that band topology follows from a unified real-space definition in terms of an obstruction towards describing topological bands using exponentially localized and symmetric Wannier functions [5, 6]. In contrast, trivial/atomic insulators are always capable of being “Wannierized”. This definition has led to the concept of fragile topology, where a set of bands are Wannier obstructed by themselves, yet the obstruction can be removed upon coupling to certain additional trivial bands [7–13]. Practically, fragile topological bands are proposed to exist in magic-angle twisted bilayer graphene [14–16], and are engineered in photonic [17] and phononic systems [18].

Apart from static systems, topological phenomena also exist in systems far from equilibrium [19, 20]. A prototypical example is periodically driven systems that are described by Floquet theory. Floquet engineering can enable nontrivial band topology in statically trivial systems [21–24] and even achieve exotic topological phases without any static counterparts [25–27]. Existing studies, however, have only considered Floquet systems with stable Wannier obstructions [28]. It is then natural to ask whether fragile topology exists in an out-of-equilibrium setting, and whether Floquet engineering can realize such phases in statically trivial systems.

In this work, we provide an affirmative answer to the above questions by constructing two explicit lattice models, the Floquet honeycomb model and the Floquet π -flux model, to demonstrate driving-enabled Floquet fragile topology. By tuning the driving amplitudes, both models realize a variety of phases including Floquet fragile topological phases protected by crystalline rotation or mirror

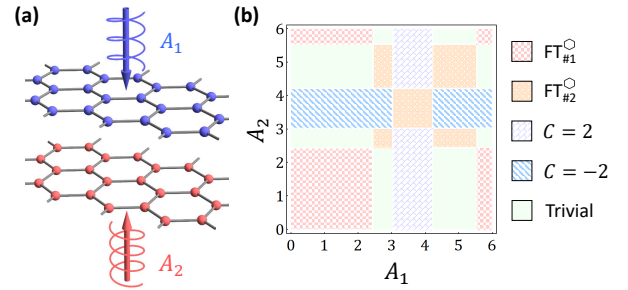


FIG. 1. (a) A schematic of the Floquet honeycomb model. “Atoms” with different colors are driven by gauge fields with different chiralities and amplitudes. (b) Phase diagram of the Floquet honeycomb model upon tuning the driving amplitudes A_1 and A_2 [29].

symmetries, Floquet Chern insulators, and trivial atomic phases. We characterize the fragile topological phases via atomic decompositions as well as the Wilson loop technique. As opposed to other phases in our models, all fragile phases carry additional higher-order topology with fractional corner charges, which serves as a unique and unambiguous boundary feature for fragile topology.

Floquet honeycomb model.— Consider a two-dimensional honeycomb lattice with two species of spinless s -orbital electrons per site:

$$H_{\square}(\tau) = - \sum_{\langle i,j \rangle, \alpha} t_{\alpha}(\tau) c_{i,\alpha}^{\dagger} c_{j,\alpha} + \Delta \sum_i c_{i,1}^{\dagger} c_{i,2} + \text{H.c.}, \quad (1)$$

where $\alpha = 1, 2$ labels the species, and the hoppings $t_{\alpha}(\tau)$ are time-dependent. The time-dependence in t_{α} originates from coupling to a time-periodic gauge field $\mathcal{A}_{\alpha}(\tau) = A_{\alpha}(\cos \omega \tau, (-1)^{\alpha} \sin \omega \tau)$ via the Peierls substitution: $t_{\alpha}(\tau) = t_0 \exp[-i \int_{\mathbf{r}_i}^{\mathbf{r}_j} \mathcal{A}_{\alpha}(\tau) \cdot d\mathbf{r}]$. Here A_{α} and ω are the amplitudes and frequency of the drive. This dynamic gauge field is physically equivalent to that of circularly polarized light [e.g. left-handed for $\alpha = 1$ and right-

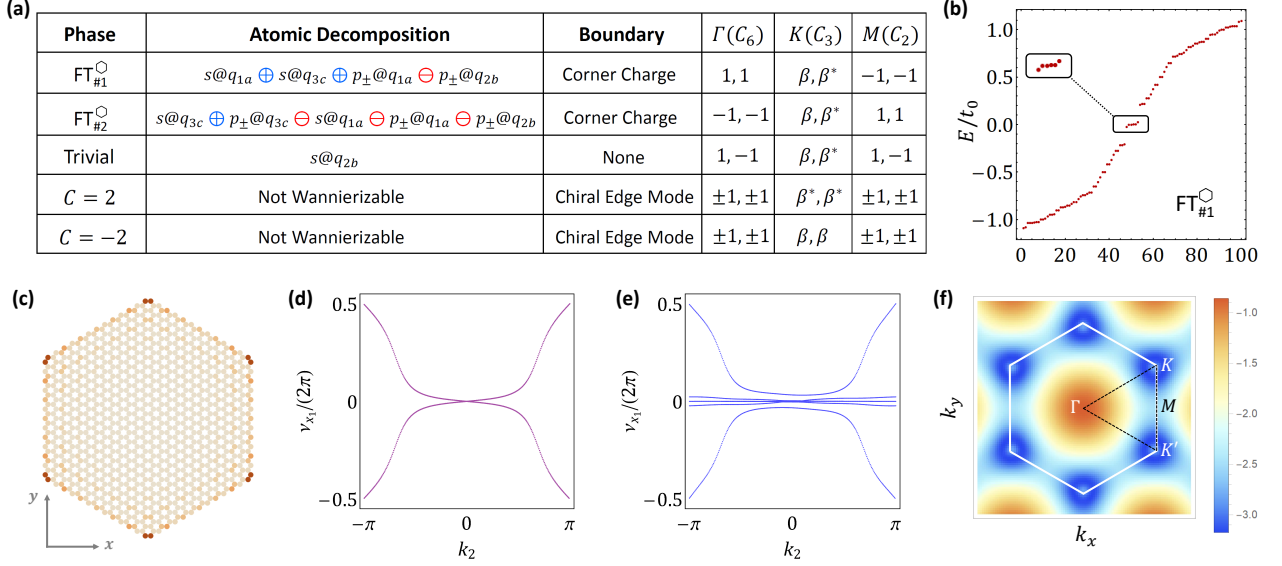


FIG. 2. (a) Atomic decompositions, boundary signatures, and symmetry data for topologically distinct phases in the Floquet honeycomb model. Here $\beta = e^{i\frac{2\pi}{3}}$. (b) and (c) Fractional corner charge modes for $\text{FT}_{\#1}^\circ$ [30]. (d) Windings of the Wilson loop spectrum of $\text{FT}_{\#1}^\circ$. k_2 is the crystal momentum along the reciprocal lattice vector. (e) Coupling to $p_{\pm}@q_{2b}$ unwinds the Wilson loop for $\text{FT}_{\#1}^\circ$. (f) Finite $\log(\det[S(\mathbf{k})])$ throughout the BZ implies no Wannier obstruction for $\text{FT}_{\#1}^\circ \oplus (p_{\pm}@q_{2b})$.

handed for $\alpha = 2$, as illustrated in Fig. 1(a)], and can be engineered in various experimental setups [21, 23, 31].

While $H_\circ(\tau)$ generally breaks all its crystalline symmetries at a fixed time τ , its corresponding effective Floquet Hamiltonian H_\circ^F generating stroboscopic time-evolutions actually restores the six-fold rotation symmetry C_6 in the high-frequency limit $\omega \gg |t_0|$ [32], where

$$H_\circ^F = h_{\tilde{t}}(A_\alpha) + h_\Delta + h_\lambda(A_\alpha, \omega) + \mathcal{O}(\omega^{-2}). \quad (2)$$

Here $h_{\tilde{t}}$ and h_Δ take the same form as in Eq. 1, now with the renormalized nearest-neighbor (NN) hopping $\tilde{t}_\alpha = t_0 \mathcal{J}_0(A_\alpha)$, where $\mathcal{J}_n(x)$ is the n -th Bessel function of the first kind. h_λ is a driving-induced Haldane-like next-nearest-neighbor (NNN) hopping term that explicitly breaks time-reversal symmetry and opens up a bulk energy gap [33]: $h_\lambda(A_\alpha, \omega) = i \sum_\alpha \sum_{\langle\langle i, j \rangle\rangle} \mu_{ij} \lambda_\alpha c_{i, \alpha}^\dagger c_{j, \alpha}$. If an electron hops to its NNN (counter-)clockwise around the hexagon center, it picks up a phase $\mu_{ij} = +1(-1)$. The NNN hopping can be analytically obtained as $\lambda_\alpha = -2t_0^2 \sum_{n=1}^{\infty} \sin \frac{2\pi n}{3} \mathcal{J}_n^2(A_\alpha) / (n\omega)$ [20]. Crucially, since \tilde{t}_α and λ_α depend on the driving amplitudes A_α through the oscillating Bessel functions, their signs can be *individually* controlled by tuning A_α , which is the key for realizing various topological phases shown in Fig. 1(b). In particular, when $\lambda_1 \lambda_2 < 0$, H_\circ^F achieves two inequivalent fragile topological phases (dubbed $\text{FT}_{\#1}^\circ$ and $\text{FT}_{\#2}^\circ$) with Wannier obstructions that can nevertheless be removed upon coupling to certain atomic bands.

To understand the nature of the Wannier obstruction, we take $\text{FT}_{\#1}^\circ$ with $\tilde{t}_{1,2} > 0$ as an example. A similar

analysis can be performed for the $\text{FT}_{\#2}^\circ$ with $\tilde{t}_{1,2} < 0$. The first evidence of the “fragile” Wannier obstruction manifests in the symmetry eigenvalues of the two occupied bands at high-symmetry momenta, as shown in Fig. 1(a). In particular, we find that no two-band atomic insulator on a honeycomb lattice shares the same set of symmetry data as $\text{FT}_{\#1}^\circ$ [32]. This clearly demonstrates an obstruction towards adiabatically connecting $\text{FT}_{\#1}^\circ$ to an atomic system with the same amount of degrees of freedom.

We now show that such Wannier obstruction in $\text{FT}_{\#1}^\circ$ can be removed upon adding additional atomic orbitals. Consider coupling $\text{FT}_{\#1}^\circ$ with a pair of p_{\pm} orbitals placed at the hexagon corners (i.e. maximal Wyckoff position q_{2b}), which we denote as “ $p_{\pm}@q_{2b}$ ” for short. Here $p_{\pm} = p_x \pm ip_y$. This composite system $\text{FT}_{\#1}^\circ \oplus (p_{\pm}@q_{2b})$ shares the same symmetry data as the following combination of atomic insulators: $(s@q_{1a}) \oplus (s@q_{3c}) \oplus (p_{\pm}@q_{1a})$, where q_{1a} and q_{3c} denote the maximal Wyckoff positions at the hexagon center and the center of each hexagon edge, respectively. This implies that the composite system $\text{FT}_{\#1}^\circ \oplus (p_{\pm}@q_{2b})$ can be Wannierized with no obstruction. We further study the Wilson loop spectrum of $\text{FT}_{\#1}^\circ$, as shown in Fig. 2(e). The Wilson loop spectrum is gapless and features nontrivial windings, a direct implication of Wannier obstruction [10, 34]. On the other hand, when coupled to additional orbitals $p_{\pm}@q_{2b}$, the Wilson loop for the composite system indeed unwinds and becomes gapped, as shown in Fig. 2(f). This again signals the Wannierizability of the composite sys-

tem $\text{FT}_{\#1}^{\square} \oplus (p_{\pm} @ q_{2b})$.

Finally, we construct a set of localized trial Wannier basis $|w_l(\mathbf{r})\rangle$ ($l = 1, \dots, 6$) for $(s @ q_{1a}) \oplus (s @ q_{3c}) \oplus (p_{\pm} @ q_{1a})$, by superposing the tight-binding basis of H_{\square}^F . We provide the explicit expressions of $|w_l(\mathbf{k})\rangle$, the Fourier transform of $|w_l(\mathbf{r})\rangle$, in [32]. We now follow the procedure in Ref. [5] and define an overlap matrix $\mathcal{S}_{ll'}(\mathbf{k}) = \langle \Phi_l(\mathbf{k}) | \Phi_{l'}(\mathbf{k}) \rangle$, where $|\Phi_l(\mathbf{k})\rangle$ is constructed by projecting our trial basis $|w_l(\mathbf{k})\rangle$ onto the occupied states of $\text{FT}_{\#1}^{\square} \oplus (p_{\pm} @ q_{2b})$. In Fig. 2(g), we map out (the logarithm of) $\det[\mathcal{S}(\mathbf{k})]$ for $\text{FT}_{\#1}^{\square} \oplus (p_{\pm} @ q_{2b})$ and find $\det[\mathcal{S}(\mathbf{k})] \neq 0$ throughout the Brillouin zone (BZ), indicating no obstruction towards a Wannier representation with $|w_l(\mathbf{k})\rangle$ for our target system. This unambiguously proves the Wannierizability of $\text{FT}_{\#1}^{\square} \oplus (p_{\pm} @ q_{2b})$ and its adiabatic equivalence to $(s @ q_{1a}) \oplus (s @ q_{3c}) \oplus (p_{\pm} @ q_{1a})$. Formally, $\text{FT}_{\#1}^{\square}$ can be decomposed into a superposition of atomic insulators as

$$\text{FT}_{\#1}^{\square} \equiv (s @ q_{1a}) \oplus (s @ q_{3c}) \oplus (p_{\pm} @ q_{1a}) \ominus (p_{\pm} @ q_{2b}), \quad (3)$$

where the atomic subtraction “ \ominus ” indicates the fragile topological nature of $\text{FT}_{\#1}^{\square}$. We emphasize that the fragile topology here is protected by the C_6 symmetry, resembling a Floquet version of the “shift insulator” [12]. In [32], we show that breaking C_6 down to C_3 will necessarily spoil the fragile topology in our system.

When $\lambda_1 \lambda_2 < 0$ and $\tilde{t}_1 \tilde{t}_2 < 0$, H_{\square}^F is trivially atomic, equivalent to $s @ q_{2b}$, with a gapped boundary. When $\lambda_1 \lambda_2 > 0$, both electrons species carry identical Chern numbers $|\mathcal{C}_{1,2}| = 1$, leading to a Chern insulator phase for H_{\square}^F with $\mathcal{C} = \pm 2$. Such a Chern insulator hosts a pair of chiral edge modes circulating along the system boundary, with the chirality (i.e. the sign of \mathcal{C}_{α}) determined by the sign of λ_{α} .

Remarkably, both fragile phases are in fact *higher-order topological*, which feature in-gap fractional corner charges $\frac{e}{6} \pmod{e}$ in a finite system with C_6 symmetric boundary, as is numerically confirmed in Fig. 2(b)&(d). The fractional quantization of the corner charge can be understood from our atomic decomposition, along with the fact that atomic insulators with orbitals on q_{2b} and q_{3c} host corner charges of $\frac{2e}{3}$ and $\frac{e}{2}$, respectively [35]. The presence of robust corner charge modes clearly distinguishes $\text{FT}_{\#1,2}^{\square}$ from both the Chern insulator phases and the trivial phase, and thus serves as a clear experimental indicator of fragile topology in our model.

Floquet π -flux model.— We now present a second example with tunable fragile topology under periodic driving. Consider a square lattice with π -flux penetrating each elementary plaquette, with the Hamiltonian $h_{\square} = \sum_{\langle ij \rangle} t_{ij} c_i^{\dagger} c_j + \text{H.c.}$. We choose the gauge such that the NN hoppings $t_{ij} = t$ on horizontal bonds, and $t_{ij} = \pm it$ on vertical bonds, as shown in Fig. 3(a). In the absence of driving, the energy spectrum of the π -flux model takes the form: $E_{\mathbf{k}} = \pm 2t \sqrt{\cos^2 k_x + \sin^2 k_y}$ where

$\mathbf{k} \in [-\frac{\pi}{2}, \frac{\pi}{2}] \times [-\pi, \pi)$. The spectrum has two Dirac nodes at high-symmetry points X and M in the BZ. Similarly to the honeycomb model, the π -flux model is coupled to a time-dependent gauge field $Ae^{i\omega\tau}$ via the Peierls substitution. In the high-frequency limit, we show that the effective Floquet Hamiltonian to order $1/\omega$ is given by [32]:

$$h_{\square}^F = \sum_{\langle ij \rangle} t_{1,ij} c_i^{\dagger} c_j + \sum_{\langle\langle ij \rangle\rangle} t_{2,ij} c_i^{\dagger} c_j + \text{H.c.} + \mathcal{O}(\omega^{-2}), \quad (4)$$

where the renormalized NN hopping and the driving-induced NNN hopping are given by $t_{1,ij} = t_{ij} \mathcal{J}_0(A)$ and $t_{2,ij} = \frac{4\eta_{ij} t^2}{\omega} \sum_{m>0} \frac{\mathcal{J}_m^2(A)}{m} \sin(\frac{\pi}{2} m)$. The NNN hopping has alternating signs $\eta_{ij} = \pm 1$ as illustrated in Fig. 3(a). In the presence of t_2 , each triangle in Fig. 3 has a flux $\pm \frac{\pi}{2}$ which breaks time-reversal symmetry and opens up a gap at the Dirac points, yielding two bands carrying Chern numbers $\mathcal{C} = \pm 1$ [36].

Consider coupling two copies of the π -flux model with s -orbital electrons of *opposite* spins under oppositely polarized drives:

$$H_{\square}^F = h_{\square,\uparrow}^F(t, A_1 e^{-i\omega\tau}) + h_{\square,\downarrow}^F(-t, A_2 e^{i\omega\tau}) + H_g, \quad (5)$$

where $\pm t$ denotes the NN hoppings of the undriven model, and H_g is the coupling between two copies, whose explicit form will be specified below. Hamiltonian (5) has a C_2 rotation symmetry with the rotation center being the bond center. Once again, the signs and values of NN and NNN hoppings in each copy $\{t_{1\uparrow}, t_{2\uparrow}, t_{1\downarrow}, t_{2\downarrow}\}$ can be varied by tuning the two driving amplitudes A_1 and A_2 , such that Hamiltonian (5) realizes a variety of phases with distinct boundary signatures. In Fig. 3(b)&(c), we show the phase diagram of Hamiltonian (3) upon tuning A_1 and A_2 , as well as their boundary signatures.

For $t_{1\uparrow} t_{1\downarrow} < 0$, $t_{2\uparrow} t_{2\downarrow} < 0$, Hamiltonian (5) realizes C_2 -protected fragile topology. This further splits into two distinct phases which we label as $\text{FT}_{\#1}^{\square}$ and $\text{FT}_{\#2}^{\square}$, as shown in Fig. 3(b). Since t_2 has opposite signs in the two copies, the two occupied bands carry Chern numbers $\mathcal{C} = \pm 1$, and host two counter-propagating chiral edge modes. However, since the total Chern number vanishes, these chiral edge modes can be gapped out by adding C_2 -preserving couplings between the two copies $H_g = \sum_{i \in \Lambda_o} g_1 (c_{i\uparrow}^{\dagger} c_{i\downarrow} - c_{i+\hat{x}\uparrow}^{\dagger} c_{i+\hat{x}\downarrow}) + g_2 (c_{i\uparrow}^{\dagger} c_{i+\hat{x}\downarrow} - c_{i\downarrow}^{\dagger} c_{i+\hat{x}\uparrow}) + \text{H.c.}$, where Λ_o denotes the sublattice belonging to odd columns, and site $i + \hat{x}$ belongs to even columns. By constructing the low-energy effective edge theory [32], one can show that the edge spectrum indeed becomes gapped upon adding H_g . Hamiltonian (5) thus realizes an insulator without anomalous edge modes. Nonetheless, it suffers from an obstruction towards a Wannier representation. In Fig. 3(b), we list the C_2 eigenvalues at high symmetry momenta for $\text{FT}_{\#1}^{\square}$ and $\text{FT}_{\#2}^{\square}$. We find that these symmetry representations cannot be realized with any two-band atomic insulator and

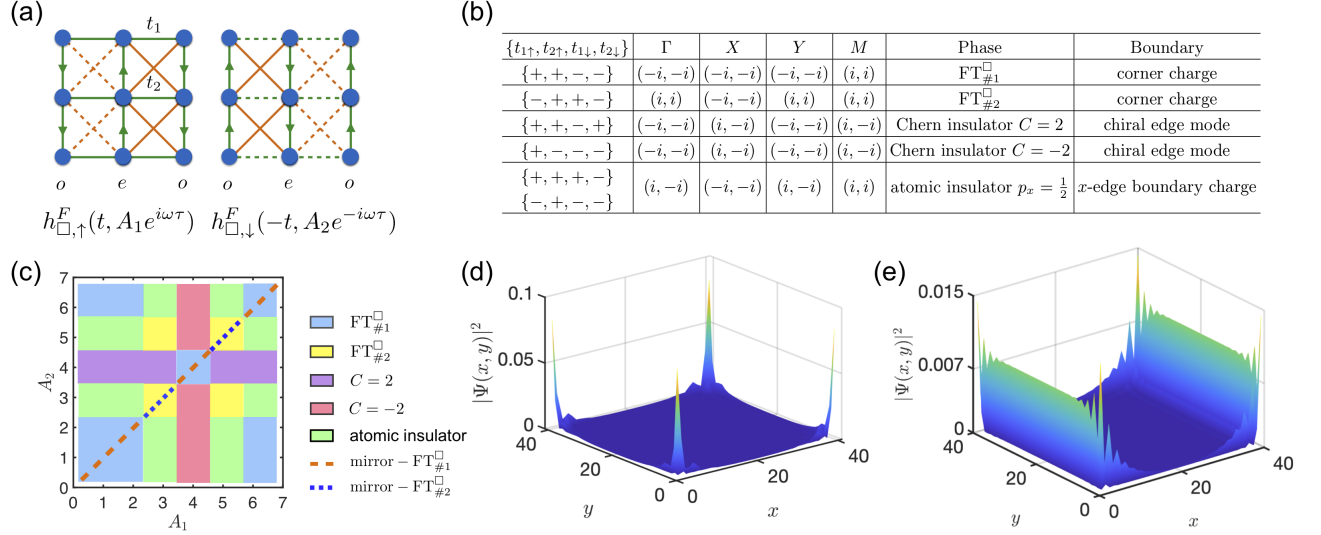


FIG. 3. (a) FT insulator constructed by coupling two copies of the π -flux model with opposite spins and oppositely polarized drives. Fermions hopping across the solid lines, dotted lines, and along the arrows will pick up a phase of 0, π , and $\frac{\pi}{2}$, respectively. (b) C_2 eigenvalues at high symmetry momenta, the corresponding phases, as well as their boundary signatures. $\{\pm\}$ denotes the sign of each hopping term. (c) Phase diagram of Hamiltonian (5) upon tuning A_1 and A_2 . (d) Corner charge in the mirror- $\text{FT}_{\#1}^{\square}$ phase. (e) Boundary charge in the atomic insulator phase with $\mathbf{P} = (\frac{1}{2}, 0)$.

hence the system is Wannier obstructed. The Wannier obstruction can also be detected from the Wilson loop spectrum. In fact, the symmetry data of $\text{FT}_{\#1}^{\square}$ and $\text{FT}_{\#2}^{\square}$ in Fig. 3(b) enforce nontrivial windings of the Wilson loop spectrum [37], which we verify numerically [32].

Next, we show that the Wannier obstruction is fragile and can be removed upon adding atomic orbitals to Hamiltonian (5). Consider coupling $\text{FT}_{\#1}^{\square}$ to two spin-up orbitals per unit cell at C_2 -symmetric positions: $(0, \frac{1}{4})$ away from the odd sublattice and $(0, -\frac{1}{4})$ away from the even sublattice. We find that the new composite system shares the same symmetry data as the atomic insulator: $(s_{\uparrow} @ q_{1a}) \oplus (s_{\uparrow} @ q_{1b}) \oplus (s_{\uparrow} @ q_{1c}) \oplus (s_{\downarrow} @ q_{1d})$, indicating that the composite system has no Wannier obstruction. Here the maximal Wyckoff positions for a C_2 -symmetric unit cell are: $q_{1a} = (0, 0)$, $q_{1b} = (\frac{1}{2}, 0)$, $q_{1c} = (0, \frac{1}{2})$, $q_{1d} = (\frac{1}{2}, \frac{1}{2})$. Furthermore, we show in [32] that the Wilson loop unwinds upon coupling to the added atomic orbitals. Taken together, the Wannier obstructions in $\text{FT}_{\#1}^{\square}$ and $\text{FT}_{\#2}^{\square}$ are indeed fragile.

Along the line $A_1 = A_2$ in Fig. 3(c), the system has two additional mirror symmetries M_x and M_y [38]. Under the basis $(c_{o\uparrow}^{\dagger}, c_{e\uparrow}^{\dagger}, c_{o\downarrow}^{\dagger}, c_{e\downarrow}^{\dagger})$, these two symmetries can be written as: $M_x = -i\sigma^y \otimes \gamma^y$ and $M_y = i\sigma^z \otimes \gamma^x$ with $[M_x, M_y] = 0$, where the Pauli matrices σ^a and γ^b act on sublattice and spin degrees of freedom respectively. The mirror symmetries protect *two distinct new fragile topological phases*: mirror- $\text{FT}_{\#1}^{\square}$ and mirror- $\text{FT}_{\#2}^{\square}$, whose M_x and M_y representations cannot be realized in any atomic insulator. We provide the atomic decompositions

in the presence of mirror symmetries in [32]. Remarkably, mirror- $\text{FT}_{\#1}^{\square}$ and mirror- $\text{FT}_{\#2}^{\square}$ host four corner modes with charge $\frac{e}{4} \pmod{e}$ [Fig. 3(d)], which can be seen from the atomic decomposition and the filling anomaly [35]. These corner charges persist for $\text{FT}_{\#1}^{\square}$ and $\text{FT}_{\#2}^{\square}$ when A_1 and A_2 are slightly off the mirror-symmetric line. Nonetheless, when $M_{x,y}$ are strongly broken, C_2 symmetry alone will generically protect only two corner charges $\frac{e}{2} \pmod{e}$ for $\text{FT}_{\#1}^{\square}$ and $\text{FT}_{\#2}^{\square}$.

When $t_{2\uparrow}t_{2\downarrow} > 0$, the occupied bands of H_{\square} have a net Chern number $\mathcal{C} = \pm 2$, hence realize a Chern insulator with two chiral edge modes at the boundary. Finally, when $t_{1\uparrow}t_{1\downarrow} > 0$, $t_{2\uparrow}t_{2\downarrow} < 0$, H_{\square} realizes an atomic insulator $(s_{\uparrow} @ q_{1c}) \oplus (s_{\downarrow} @ q_{1d})$, which has a nonzero bulk polarization $\mathbf{P} = (\frac{1}{2}, 0)$. Consequently, this atomic insulator has charge accumulation along edges parallel to the y -direction, but not on the other edges [Fig. 3(e)]. Therefore, similar to the honeycomb model, different phases of the π -flux model can also be diagnosed solely from their boundary signatures.

Discussions - We present two examples of Floquet systems exhibiting driving-induced tunable Floquet fragile topology with characteristic boundary features. Floquet systems are advantageous in their tunability, which offers a unique opportunity to explore the topological quantum criticality for fragile topology in experiments. Although both of our models are statically semimetallic, one may as well start from static gapped systems. Meanwhile, general fragile topological phases are recently proposed to host in-gap spectral flows under twisted boundary conditions in real space [13, 18]. For Floquet fragile topolog-

ical systems, we expect that the Floquet drive acts as an on-off controller of the twisted-boundary-induced spectral flows. A detailed discussion will be left for future studies.

Floquet Haldane phase, the key ingredient of our honeycomb model, has already been proposed and realized in a variety of experimental settings, including photonic waveguides [23], cold atoms [31], and acoustic crystals [39]. To realize our Floquet honeycomb model, for example, one can simply stack two layers of the acoustic Floquet Haldane system proposed in Ref. [39] with layer-dependent drives, and further introduce an additional acoustic waveguide at each site to bridge between the layers, which mimics the interlayer coupling Δ . With the state-of-the-art fabrication techniques in the metamaterial platforms, it is conceivable that fragile topology in out-of-equilibrium systems that we propose in this work can be realized experimentally in the near future.

Acknowledgment.— We thank Eslam Khalaf, Jiabin Yu and Mohammad Hafezi for helpful discussions. We thank S. Das Sarma for a critical reading of the manuscript and useful feedback. R.-X.Z. is supported by a JQI Postdoctoral Fellowship, the Laboratory for Physical Sciences and Microsoft. Z.-C. Y. acknowledges funding by the DoE BES Materials and Chemical Sciences Research for Quantum Information Science program (award No. DE-SC0019449), DoE ASCR FAR-QC (award No. DE-SC0020312), DoE ASCR Quantum Testbed Pathfinder program (award No. DE-SC0019040), NSF PFCQC program, AFOSR MURI, AFOSR, ARO MURI, ARL CDQI, and NSF PFC at JQI. Z.-C. Y. is also supported by AFOSR MURI FA9550-19-1-0399 and ONR MURI.

* ruixing@umd.edu

† zcyang@umd.edu

- [1] M. Z. Hasan and C. L. Kane, Colloquium: Topological insulators, *Rev. Mod. Phys.* **82**, 3045 (2010).
- [2] X.-L. Qi and S.-C. Zhang, Topological insulators and superconductors, *Rev. Mod. Phys.* **83**, 1057 (2011).
- [3] D. J. Thouless, M. Kohmoto, M. P. Nightingale, and M. den Nijs, Quantized hall conductance in a two-dimensional periodic potential, *Phys. Rev. Lett.* **49**, 405 (1982).
- [4] C. L. Kane and E. J. Mele, Z_2 topological order and the quantum spin hall effect, *Phys. Rev. Lett.* **95**, 146802 (2005).
- [5] A. A. Soluyanov and D. Vanderbilt, Wannier representation of z_2 topological insulators, *Phys. Rev. B* **83**, 035108 (2011).
- [6] B. Bradlyn, L. Elcoro, J. Cano, M. G. Vergniory, Z. Wang, C. Felser, M. I. Aroyo, and B. A. Bernevig, Topological quantum chemistry, *Nature* **547**, 298 (2017).
- [7] H. C. Po, H. Watanabe, and A. Vishwanath, Fragile topology and wannier obstructions, *Phys. Rev. Lett.* **121**, 126402 (2018).
- [8] B. Bradlyn, Z. Wang, J. Cano, and B. A. Bernevig, Disconnected elementary band representations, fragile topology, and wilson loops as topological indices: An example on the triangular lattice, *Phys. Rev. B* **99**, 045140 (2019).
- [9] Y. Hwang, J. Ahn, and B.-J. Yang, Fragile topology protected by inversion symmetry: Diagnosis, bulk-boundary correspondence, and wilson loop, *Phys. Rev. B* **100**, 205126 (2019).
- [10] A. Bouhon, A. M. Black-Schaffer, and R.-J. Slager, Wilson loop approach to fragile topology of split elementary band representations and topological crystalline insulators with time-reversal symmetry, *Phys. Rev. B* **100**, 195135 (2019).
- [11] Z. Song, L. Elcoro, N. Regnault, and B. A. Bernevig, Fragile phases as affine monoids: Full classification and material examples, *arXiv preprint arXiv:1905.03262* (2019).
- [12] S. Liu, A. Vishwanath, and E. Khalaf, Shift insulators: Rotation-protected two-dimensional topological crystalline insulators, *Phys. Rev. X* **9**, 031003 (2019).
- [13] Z.-D. Song, L. Elcoro, and B. A. Bernevig, Twisted bulk-boundary correspondence of fragile topology, *Science* **367**, 794 (2020).
- [14] H. C. Po, L. Zou, T. Senthil, and A. Vishwanath, Faithful tight-binding models and fragile topology of magic-angle bilayer graphene, *Phys. Rev. B* **99**, 195455 (2019).
- [15] J. Ahn, S. Park, and B.-J. Yang, Failure of nielsen-ninomiya theorem and fragile topology in two-dimensional systems with space-time inversion symmetry: Application to twisted bilayer graphene at magic angle, *Phys. Rev. X* **9**, 021013 (2019).
- [16] Z. Song, Z. Wang, W. Shi, G. Li, C. Fang, and B. A. Bernevig, All magic angles in twisted bilayer graphene are topological, *Phys. Rev. Lett.* **123**, 036401 (2019).
- [17] M. B. de Paz, M. G. Vergniory, D. Bercioux, A. García-Etxarri, and B. Bradlyn, Engineering fragile topology in photonic crystals: Topological quantum chemistry of light, *Phys. Rev. Research* **1**, 032005 (2019).
- [18] V. Peri, Z.-D. Song, M. Serra-Garcia, P. Engeler, R. Queiroz, X. Huang, W. Deng, Z. Liu, B. A. Bernevig, and S. D. Huber, Experimental characterization of fragile topology in an acoustic metamaterial, *Science* **367**, 797 (2020).
- [19] J. Cayssol, B. Dóra, F. Simon, and R. Moessner, Floquet topological insulators, *physica status solidi (RRL)—Rapid Research Letters* **7**, 101 (2013).
- [20] T. Oka and S. Kitamura, Floquet engineering of quantum materials, *Annual Review of Condensed Matter Physics* **10**, 387 (2019).
- [21] N. H. Lindner, G. Refael, and V. Galitski, Floquet topological insulator in semiconductor quantum wells, *Nature Physics* **7**, 490 (2011).
- [22] L. Jiang, T. Kitagawa, J. Alicea, A. R. Akhmerov, D. Pekker, G. Refael, J. I. Cirac, E. Demler, M. D. Lukin, and P. Zoller, Majorana fermions in equilibrium and in driven cold-atom quantum wires, *Phys. Rev. Lett.* **106**, 220402 (2011).
- [23] M. C. Rechtsman, J. M. Zeuner, Y. Plotnik, Y. Lumer, D. Podolsky, F. Dreisow, S. Nolte, M. Segev, and A. Szameit, Photonic floquet topological insulators, *Nature* **496**, 196 (2013).
- [24] G. Usaj, P. M. Perez-Piskunow, L. E. F. Foa Torres, and C. A. Balseiro, Irradiated graphene as a tunable floquet topological insulator, *Phys. Rev. B* **90**, 115423 (2014).
- [25] T. Kitagawa, E. Berg, M. Rudner, and E. Demler, Topo-

- logical characterization of periodically driven quantum systems, *Phys. Rev. B* **82**, 235114 (2010).
- [26] M. S. Rudner, N. H. Lindner, E. Berg, and M. Levin, Anomalous edge states and the bulk-edge correspondence for periodically driven two-dimensional systems, *Phys. Rev. X* **3**, 031005 (2013).
- [27] P. Titum, E. Berg, M. S. Rudner, G. Refael, and N. H. Lindner, Anomalous floquet-anderson insulator as a nonadiabatic quantized charge pump, *Phys. Rev. X* **6**, 021013 (2016).
- [28] M. Nakagawa, R.-J. Slager, S. Higashikawa, and T. Oka, Wannier representation of floquet topological states, *Phys. Rev. B* **101**, 075108 (2020).
- [29] The topological phase diagram is mapped in the weakly coupling limit $\Delta \rightarrow 0$. Including a finite Δ will quantitatively modify the phase diagram.
- [30] The parameters for Floquet honeycomb model are $t_0 = 2$, $A = 1.7$, $\omega = 15$. When calculating the corner charge modes, we have artificially enlarged the energy gap to overcome the finite size effect.
- [31] G. Jotzu, M. Messer, R. Desbuquois, M. Lebrat, T. Uehlinger, D. Greif, and T. Esslinger, Experimental realization of the topological haldane model with ultracold fermions, *Nature* **515**, 237 (2014).
- [32] See Supplemental Material, which includes Refs. [12, 20, 40].
- [33] F. D. M. Haldane, Model for a quantum hall effect without landau levels: Condensed-matter realization of the "parity anomaly", *Phys. Rev. Lett.* **61**, 2015 (1988).
- [34] A. Alexandradinata, X. Dai, and B. A. Bernevig, Wilson-loop characterization of inversion-symmetric topological insulators, *Phys. Rev. B* **89**, 155114 (2014).
- [35] W. A. Benalcazar, T. Li, and T. L. Hughes, Quantization of fractional corner charge in C_n -symmetric higher-order topological crystalline insulators, *Phys. Rev. B* **99**, 245151 (2019).
- [36] X. G. Wen, F. Wilczek, and A. Zee, Chiral spin states and superconductivity, *Phys. Rev. B* **39**, 11413 (1989).
- [37] A. Alexandradinata, X. Dai, and B. A. Bernevig, Wilson-loop characterization of inversion-symmetric topological insulators, *Phys. Rev. B* **89**, 155114 (2014).
- [38] We note that the Floquet honeycomb model also possesses in-plane mirror symmetries along $A_1 = A_2$ that provide additional symmetry protections to the fragile topology. Such mirror symmetries can be removed by including a species-dependent on-site potential.
- [39] R. Fleury, A. B. Khanikaev, and A. Alu, Floquet topological insulators for sound, *Nature communications* **7**, 1 (2016).
- [40] M. Bukov, L. D'Alessio, and A. Polkovnikov, Universal high-frequency behavior of periodically driven systems: from dynamical stabilization to floquet engineering, *Advances in Physics* **64**, 139 (2015).

Supplemental Material for "Tunable Fragile Topology in Floquet Systems"

Appendix A: Symmetry Properties of Floquet Honeycomb Model

Symmetry of Static Honeycomb Model

We start by briefly reviewing the symmetry properties of the Floquet honeycomb model in the zero driving limit $A_{1,2} \rightarrow 0$. In this case, the model Hamiltonian resembles that of a A - A stacked bilayer graphene. In momentum space, we have

$$H_{\odot}^s(\mathbf{k}) = -t_0(\text{Re}[f(\mathbf{k})]\mu_0 \otimes \sigma_x + \text{Im}[f(\mathbf{k})]\mu_0 \otimes \sigma_y) + \Delta\mu_x \otimes \sigma_0, \quad (6)$$

where the superscript "s" indicates the static limit. We have defined the nearest-neighbor hopping function $f(\mathbf{k}) = \sum_{i=1}^3 e^{-i\mathbf{k} \cdot \delta_i}$ with $\delta_1 = \frac{1}{2}(1, \sqrt{3})$, $\delta_2 = \frac{1}{2}(1, -\sqrt{3})$, and $\delta_3 = (-1, 0)$. The Pauli matrices μ_i and σ_i ($i = 0, x, y, z$) act on the species and sublattice degrees of freedom, respectively.

We will focus on rotational symmetries and ignore the mirror symmetries of the system, since they will be explicitly broken even in the high-frequency limit. The six-fold rotation $C_6 = \mu_0 \otimes \sigma_x$ exchanges the two sublattices of the honeycomb lattice and $H_{\odot}^s(\mathbf{k})$ transforms under C_6 as

$$C_6 H_{\odot}^s(\mathbf{k}) C_6^\dagger = H_{\odot}^s(R_6 \mathbf{k}), \quad (7)$$

with

$$R_n = \begin{pmatrix} \cos \frac{2\pi}{n} & -\sin \frac{2\pi}{n} \\ \sin \frac{2\pi}{n} & \cos \frac{2\pi}{n} \end{pmatrix}. \quad (8)$$

In the Brillouin zone, $\Gamma = (0, 0)$ is invariant under C_6 . We have two inequivalent $K = \frac{2\pi}{3\sqrt{3}}(\sqrt{3}, 1)$ and $K' = \frac{2\pi}{3\sqrt{3}}(\sqrt{3}, -1)$ that have little group C_3 . In addition, there are three $M = \frac{2\pi}{3}(1, 0)$, $M' = \frac{2\pi}{3}(1, \sqrt{3})$, and $M'' = \frac{2\pi}{3}(-1, \sqrt{3})$ that are invariant under C_2 . The reciprocal lattice vectors for the honeycomb lattice are given by

$$\mathbf{G}_1 = \frac{2\pi}{3}(1, \sqrt{3}), \quad \mathbf{G}_2 = \frac{2\pi}{3}(1, -\sqrt{3}). \quad (9)$$

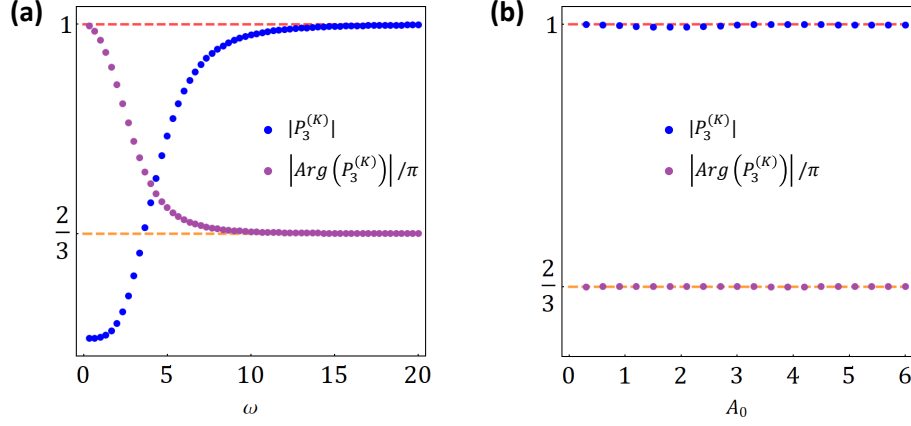


FIG. 4. Effect of lattice symmetry breaking as a function of (a) ω with a fixed $A_0 = 1.7$; and (b) A_0 with a fixed $\omega = 15$.

It is easy to check that $H_{\odot}^s(\mathbf{k} + n_1 \mathbf{G}_1 + n_2 \mathbf{G}_2) \neq H_{\odot}^s(\mathbf{k})$. To make the Hamiltonian invariant under a shift of reciprocal lattice vectors, we consider a unitary transformation $V(\mathbf{k})$

$$\tilde{H}_{\odot}^s(\mathbf{k}) = V(\mathbf{k}) H_{\odot}^s(\mathbf{k}) V(\mathbf{k})^\dagger. \quad (10)$$

where

$$V(\mathbf{k}) = \mu_x \otimes \begin{pmatrix} e^{-i\mathbf{k} \cdot \mathbf{t}_A} & 0 \\ 0 & e^{-i\mathbf{k} \cdot \mathbf{t}_B} \end{pmatrix}. \quad (11)$$

Physically, this gauge choice corresponds to choosing the hexagonal center as the unit cell origin. For a given rotation symmetry C_n , we have

$$\begin{aligned} \tilde{H}_{\odot}^s(R_n \mathbf{k}) &= V(R_n \mathbf{k}) C_n V(\mathbf{k})^\dagger V(\mathbf{k}) H_{\odot}^s(\mathbf{k}) V(\mathbf{k})^\dagger V(\mathbf{k}) C_n^\dagger V(R_n \mathbf{k})^\dagger \\ &= V(R_n \mathbf{k}) C_n V(\mathbf{k})^\dagger \tilde{H}_{\odot}^s(\mathbf{k}) V(\mathbf{k}) C_n^\dagger V(R_n \mathbf{k})^\dagger \\ &= \tilde{C}_n \tilde{H}_{\odot}^s(\mathbf{k}) \tilde{C}_n^\dagger. \end{aligned} \quad (12)$$

Therefore, the six-fold rotation operation under the new basis is

$$\tilde{C}_6(\mathbf{k}) = V(R_6 \mathbf{k}) C_6 V(\mathbf{k})^\dagger = \mu_0 \otimes \begin{pmatrix} 0 & e^{-\frac{i}{2}(3k_x - \sqrt{3}k_y)} \\ 1 & 0 \end{pmatrix}. \quad (13)$$

Similarly, the three-fold and two-fold rotation operations under the new basis are

$$\begin{aligned} \tilde{C}_3(\mathbf{k}) &= V(R_3 \mathbf{k}) C_3 V(\mathbf{k})^\dagger = \mu_0 \otimes \begin{pmatrix} e^{i\sqrt{3}k_y} & 0 \\ 0 & e^{-\frac{i}{2}(3k_x - \sqrt{3}k_y)} \end{pmatrix}, \\ \tilde{C}_2(\mathbf{k}) &= V(R_2 \mathbf{k}) C_2 V(\mathbf{k})^\dagger = \mu_0 \otimes e^{i\sqrt{3}k_y} \sigma_x. \end{aligned} \quad (14)$$

We notice that

$$\tilde{C}_3 \neq \tilde{C}_6^2, \quad \tilde{C}_2 \neq \tilde{C}_6^3. \quad (15)$$

Emergent Lattice Symmetry and High Frequency Limit

As we have mentioned in the main text, the time-dependent Hamiltonian $H_{\odot}(\tau)$ explicitly breaks all crystalline symmetries at a fixed time τ . Such symmetry breaking is easy to see if we couple the dynamic gauge potential $\mathbf{A}(\tau) = A_0(\cos \omega \tau, \sin \omega \tau)$ to $H_{\odot}^s(\mathbf{k})$ via a minimal coupling,

$$\mathbf{k} \rightarrow \mathbf{k} + \mathbf{A}(\tau). \quad (16)$$

Back in real space, the effective Floquet Hamiltonian for the honeycomb model is approximated via a high-frequency expansion [20]

$$H_{\square}^F = H_{\square}^{(0)} + \frac{[H_{\square}^{(1)}, H_{\square}^{(-1)}]}{\omega} + \mathcal{O}(\frac{1}{\omega^2}), \quad (17)$$

where we have defined

$$H_{\square}^{(n)} = \int_0^T H_{\square}(\tau) e^{in\omega\tau} d\tau. \quad (18)$$

Evaluating the above expression explicitly, we arrive at the H_{\square}^F shown in the main text, which apparently has C_6 rotation symmetry.

To visualize how the rotation symmetry gradually emerges in the Floquet Hamiltonian as one increases the driving frequency, we write our Hamiltonian in frequency space, which now becomes an infinite-dimensional matrix,

$$H_{\square}^F = \begin{pmatrix} \ddots & & & & & & \\ & H_{\square}^{(1)} & & H_{\square}^{(-1)} & & & \\ & H_{\square}^{(2)} & H_{\square}^{(0)} - (m-1)\omega & H_{\square}^{(-1)} & H_{\square}^{(-2)} & & \\ & & H_{\square}^{(1)} & H_{\square}^{(0)} - m\omega & H_{\square}^{(-1)} & H_{\square}^{(-2)} & \\ & & H_{\square}^{(2)} & H_{\square}^{(1)} & H_{\square}^{(0)} - (m+1)\omega & H_{\square}^{(-1)} & \\ & & & H_{\square}^{(2)} & H_{\square}^{(1)} & \ddots & \end{pmatrix}. \quad (19)$$

For practical purpose, we truncate the frequency space Hamiltonian up to $N\omega$ with $N \gg 1$. To quantify the rotation symmetry breaking, we consider $|\psi_K^F\rangle$, an energy eigenstate of H_{\square}^F at high symmetry point K , and evaluate

$$P_3^{(K)} = \langle \psi_K^F | C_3 | \psi_K^F \rangle. \quad (20)$$

In the high-frequency limit, we find that a C_6 -symmetric Floquet Hamiltonian will have

$$|P_3^{(K)}| = 1, \quad \frac{1}{\pi} |\text{Arg}(P_3^{(K)})| = \frac{2\pi}{3}, \quad (21)$$

As shown in Fig. 4 (a), we evaluate both the magnitude and the phase of $P_3^{(K)}$ as a function of ω . For small ω , both quantities deviate from the ideal values, which signals explicit symmetry breaking of C_6 . In particular, $P_3^{(K)}$ reaches the expected value at $\omega \sim 12$, which indicates that the system reaches the high-frequency limit. With $\omega = 15$, we also plot the $P_3^{(K)}$ as a function of $A_1 = A_2 = A_0$, which confirms that the emergent C_6 symmetry remains robust as we change the driving amplitude.

Appendix B: Fragile Topology in the Honeycomb model

Atomic Symmetry Data and Decomposition of Fragile Phase

In this section, we provide the symmetry data for different atomic insulators on a honeycomb lattice, based on which, we will discuss possible atomic decompositions for both fragile topological phases in the Floquet honeycomb model. By placing one atomic orbital on a maximal Wyckoff position, we obtain a corresponding atomic insulator and extract its symmetry data at high symmetry momenta. For a honeycomb lattice, there exists three inequivalent maximal Wyckoff positions: (i) the hexagon center q_{1a} ; (ii) the hexagon corner q_{2b} ; (iii) the midpoint of an hexagon edge q_{3c} . For a C_6 -symmetric spinless system, we should, in principle, consider atomic orbitals with an orbital angular momentum $l \in \{-2, -1, 0, 1, 2, 3\}$. As shown in Table. I, we list the atomic symmetry data for $l = 0$ (s -orbital) and $l = \pm 1$ (p_{\pm} -orbital) for all maximal Wyckoff positions.

To construct the atomic decomposition for the fragile topological phases, we consider a linear superposition of possible atomic insulators with integer-valued coefficients to match the symmetry data of the fragile phase. We point out that such an atomic decomposition for a given fragile phase is not necessarily unique. In other words, one can

Atomic Insulator	(s@1a)	(s@2b)	(s@3c)	(p _± @1a)	(p _± @2b)	(p _± @3c)
Γ (C ₆)	1	±1	1, β, β*	α, α*	α, α*, β, β*	-1, α, α* -1, α, α*
K (C ₃)	1	β, β*	1, β, β*	β, β*	1, 1, β, β*	1, β, β* 1, β, β*
M (C ₂)	1	±1	1, -1, -1	-1, -1	±1, ±1	-1, 1, 1 -1, 1, 1

TABLE I. Symmetry data for atomic orbitals on a honeycomb lattice. $\alpha = e^{i\frac{\pi}{3}}$, $\beta = e^{i\frac{2\pi}{3}}$.

couple a fragile phase with different combinations of atomic orbitals to remove the Wannier obstruction. For example, we find two inequivalent decomposition schemes for the $\text{FT}_{\#2}^\odot$ phase by considering *only* s -orbital and p_\pm orbitals,

$$\begin{aligned}\text{FT}_{\#2}^\odot &\equiv (s@q_{2b}) \oplus (s@q_{2b}) \oplus (p_\pm@q_{2b}) \oplus (s@q_{1a}) \oplus (s@q_{3c}) \oplus (p_\pm@q_{1a}) \\ &\equiv (s@q_{3c}) \oplus (p_\pm@q_{3c}) \oplus (s@q_{1a}) \oplus (p_\pm@q_{1a}) \oplus (p_\pm@q_{2b})\end{aligned}\quad (22)$$

For the first decomposition, we require adding six additional atomic orbitals $(s@q_{1a}) \oplus (s@q_{3c}) \oplus (p_\pm@q_{1a})$ to make $\text{FT}_{\#2}^\odot$ Wannierizable, while the second decomposition requires adding seven atomic orbitals $(s@q_{1a}) \oplus (p_\pm@q_{1a}) \oplus (p_\pm@q_{2b})$ to trivialize $\text{FT}_{\#2}^\odot$. One could in principle find more decomposition schemes if atomic orbitals with higher angular momenta are considered as well.

Trial Wannier Basis for $\text{FT}_{\#1}^\odot \oplus (p_\pm@q_{2b})$

In this section, we provide detailed expressions for the trial Wannier basis $|w_l\rangle$ ($l = 1, 2, \dots, 6$) for $\text{FT}_{\#1}^\odot \oplus (p_\pm@q_{2b})$ that are used to show the absence of Wannier obstruction [e.g. Fig. 2(f) in the main text]. This choice of Wannier basis is inspired by the ones in Ref. [12]. We expect the trial Wannier basis to satisfy the following requirements:

- $|w_l\rangle$ is constructed using the original tight-binding basis of $\text{FT}_{\#1}^\odot \oplus (p_\pm@q_{2b})$;
- $|w_l\rangle$ should exactly reproduce the symmetry data of $\text{FT}_{\#1}^\odot \oplus (p_\pm@q_{2b})$.

Recall that we expect

$$\text{FT}_{\#1}^\odot \oplus (p_\pm@q_{2b}) \equiv (s@q_{1a}) \oplus (s@q_{3c}) \oplus (p_\pm@q_{1a}). \quad (23)$$

Hence, the first three trial Wannier bases aim at constructing $s@q_{3c}$,

$$\begin{aligned}|w_1(\mathbf{k})\rangle &= (e^{i\mathbf{k}\cdot\mathbf{t}_A}, e^{i\mathbf{k}\cdot\mathbf{t}_B}, e^{i\mathbf{k}\cdot\mathbf{t}_A}, e^{i\mathbf{k}\cdot\mathbf{t}_B}, e^{i\mathbf{k}\cdot\mathbf{t}_A}, -e^{i\mathbf{k}\cdot\mathbf{t}_B}, e^{i\mathbf{k}\cdot\mathbf{t}_A}, -e^{i\mathbf{k}\cdot\mathbf{t}_B})^T, \\ |w_2(\mathbf{k})\rangle &= C_6|w_1(R_6^{-1}\mathbf{k})\rangle, \quad |w_3(\mathbf{k})\rangle = C_3|w_1(R_3^{-1}\mathbf{k})\rangle.\end{aligned}\quad (24)$$

The other three bases aim at constructing $s@q_{1a}$, $p_+@q_{1a}$, and $p_-@q_{1a}$, respectively.

$$\begin{aligned}|w_4(\mathbf{k})\rangle &= (0, 0, g_{0A}, g_{0B}, g_{-1A}, g_{-1B}, g_{+1A}, g_{+1B})^T, \\ |w_5(\mathbf{k})\rangle &= (g_{+1A}, g_{+1B}, g_{+1A}, g_{+1B}, g_{0A}, g_{0B}, g_{+2A}, g_{+2B})^T \\ |w_6(\mathbf{k})\rangle &= (0, 0, g_{-1A}, g_{-1B}, g_{-2A}, g_{-2B}, g_{0A}, g_{0B})^T.\end{aligned}\quad (25)$$

where we have defined

$$\begin{aligned}g_{0A} &= e^{i\mathbf{k}\cdot\mathbf{t}_A} + e^{-i\mathbf{k}\cdot\mathbf{t}_B} + e^{i\mathbf{k}\cdot(-\mathbf{t}_A+\mathbf{t}_B)}, & g_{0B} &= e^{i\mathbf{k}\cdot\mathbf{t}_B} + e^{-i\mathbf{k}\cdot\mathbf{t}_A} + e^{i\mathbf{k}\cdot(\mathbf{t}_A-\mathbf{t}_B)}, \\ g_{-1A} &= \alpha^5 e^{i\mathbf{k}\cdot\mathbf{t}_A} + \alpha^3 e^{-i\mathbf{k}\cdot\mathbf{t}_B} + \alpha e^{i\mathbf{k}\cdot(-\mathbf{t}_A+\mathbf{t}_B)}, & g_{-1B} &= e^{i\mathbf{k}\cdot\mathbf{t}_B} + \alpha^2 e^{-i\mathbf{k}\cdot\mathbf{t}_A} + \alpha^4 e^{i\mathbf{k}\cdot(\mathbf{t}_A-\mathbf{t}_B)}, \\ g_{+1A} &= \alpha e^{i\mathbf{k}\cdot\mathbf{t}_A} + \alpha^3 e^{-i\mathbf{k}\cdot\mathbf{t}_B} + \alpha^5 e^{i\mathbf{k}\cdot(-\mathbf{t}_A+\mathbf{t}_B)}, & g_{+1B} &= e^{i\mathbf{k}\cdot\mathbf{t}_B} + \alpha^4 e^{-i\mathbf{k}\cdot\mathbf{t}_A} + \alpha^2 e^{i\mathbf{k}\cdot(\mathbf{t}_A-\mathbf{t}_B)}, \\ g_{-2A} &= \alpha^4 e^{i\mathbf{k}\cdot\mathbf{t}_A} + e^{-i\mathbf{k}\cdot\mathbf{t}_B} + \alpha^2 e^{i\mathbf{k}\cdot(-\mathbf{t}_A+\mathbf{t}_B)}, & g_{-2B} &= e^{i\mathbf{k}\cdot\mathbf{t}_B} + \alpha^4 e^{-i\mathbf{k}\cdot\mathbf{t}_A} + \alpha^2 e^{i\mathbf{k}\cdot(\mathbf{t}_A-\mathbf{t}_B)}, \\ g_{+2A} &= \alpha^2 e^{i\mathbf{k}\cdot\mathbf{t}_A} + e^{-i\mathbf{k}\cdot\mathbf{t}_B} + \alpha^4 e^{i\mathbf{k}\cdot(-\mathbf{t}_A+\mathbf{t}_B)}, & g_{+2B} &= e^{i\mathbf{k}\cdot\mathbf{t}_B} + \alpha^2 e^{-i\mathbf{k}\cdot\mathbf{t}_A} + \alpha^4 e^{i\mathbf{k}\cdot(\mathbf{t}_A-\mathbf{t}_B)}\end{aligned}\quad (26)$$

where $\alpha = e^{i\frac{\pi}{3}}$ is a phase factor. It is easy to show that the above trial Wannier basis satisfy all the symmetry requirements.

Composite Hamiltonian of $\text{FT}_{\#1}^{\odot} \oplus (p_{\pm}@q_{2b})$ for Wilson Loop Calculation

To show the composite system $\text{FT}_{\#1}^{\odot} \oplus (p_{\pm}@q_{2b})$ does not have a nontrivial Wilson loop winding, we consider the following composite Hamiltonian,

$$H_{\text{composite}}(\mathbf{k}) = \begin{pmatrix} H_{\odot}^F(\mathbf{k}) & h_c \\ h_c^{\dagger} & h_{p_{\pm}@q_{2b}} \end{pmatrix} \quad (27)$$

Here, the atomic system is described by

$$h_{p_{\pm}@q_{2b}}(\mathbf{k}) = -\epsilon_F \tilde{\mu}_0 \otimes \sigma_0 - t_p \text{Re}[f(\mathbf{k})] \tilde{\mu}_0 \otimes \sigma_x - t_p \text{Im}[f(\mathbf{k})] \tilde{\mu}_0 \otimes \sigma_y, \quad (28)$$

where $\tilde{\mu}_i$ are the Pauli matrices describing p_{\pm} orbital degrees of freedom. The general 4×4 coupling matrix satisfying symmetry requirement is given by

$$h_c(\mathbf{k}) = \begin{pmatrix} v_{11}J_1(\mathbf{k}) & 0 & v_{13}J_3(\mathbf{k}) & 0 \\ 0 & v_{11}J_2(\mathbf{k}) & 0 & v_{13}J_4(\mathbf{k}) \\ v_{31}J_1(\mathbf{k}) & 0 & v_{33}J_3(\mathbf{k}) & 0 \\ 0 & v_{31}J_2(\mathbf{k}) & 0 & v_{33}J_4(\mathbf{k}) \end{pmatrix}, \quad (29)$$

where

$$\begin{aligned} J_1(\mathbf{k}) &= e^{i\mathbf{k} \cdot \mathbf{b}_1} + \alpha^4 e^{i\mathbf{k} \cdot \mathbf{b}_2} + \alpha^2 e^{i\mathbf{k} \cdot \mathbf{b}_3} \\ J_2(\mathbf{k}) &= -e^{-i\mathbf{k} \cdot \mathbf{b}_1} + \alpha e^{-i\mathbf{k} \cdot \mathbf{b}_2} + \alpha^5 e^{-i\mathbf{k} \cdot \mathbf{b}_3} \\ J_3(\mathbf{k}) &= e^{i\mathbf{k} \cdot \mathbf{b}_1} + \alpha^2 e^{i\mathbf{k} \cdot \mathbf{b}_2} + \alpha^4 e^{i\mathbf{k} \cdot \mathbf{b}_3} \\ J_4(\mathbf{k}) &= -e^{-i\mathbf{k} \cdot \mathbf{b}_1} + \alpha^5 e^{-i\mathbf{k} \cdot \mathbf{b}_2} + \alpha e^{-i\mathbf{k} \cdot \mathbf{b}_3} \end{aligned} \quad (30)$$

Here $\mathbf{b}_1 = (0, \sqrt{3})$, $\mathbf{b}_2 = (-\frac{3}{2}, -\frac{\sqrt{3}}{2})$, and $\mathbf{b}_3 = (\frac{3}{2}, -\frac{\sqrt{3}}{2})$ are the displacement vectors between next-nearest neighbors atoms. When calculating the Wilson loop spectrum in Fig. 2 (d) & (e) in the main text, we have chosen the following set of parameters

$$\Delta = 0, \epsilon_F = 4, t_p = 0.4, v_{11} = 0.8, v_{33} = 0.4, v_{13} = 0.3, v_{31} = 0.5 \quad (31)$$

No Fragile Topology for C_3 -symmetric Floquet Honeycomb Model

Now we show that when breaking the C_6 symmetry of H_{\odot}^F to C_3 by adding a sublattice staggered potential

$$h_{\text{stagger}} = \tilde{\Delta} \mu_0 \otimes \sigma_z, \quad (32)$$

the original fragile topological phase will be trivialized. This directly implies that the fragile topology here is protected by C_6 symmetry.

Take $\text{FT}_{\#1}^{\odot}$ as an example. With additional h_{stagger} and the remaining C_3 symmetry, we only need to consider the C_3 symmetry data at Γ and K . By comparing the new symmetry data of $\text{FT}_{\#1}^{\odot}$ with Table. I, we find that the new symmetry data exactly matches that of $s@q_{2b}$. To show that a C_3 -symmetric $\text{FT}_{\#1}^{\odot}$ phase is adiabatically connected to the atomic insulator $s@q_{2b}$, we consider the following trial Wannier basis $|\tilde{w}_{1,2}\rangle$ for $s@q_{2b}$,

$$\begin{aligned} |\tilde{w}_1(\mathbf{k})\rangle &= (e^{i\mathbf{k} \cdot \mathbf{t}_A}, 0, -e^{i\mathbf{k} \cdot \mathbf{t}_A}, 0)^T, \\ |\tilde{w}_2(\mathbf{k})\rangle &= (0, e^{i\mathbf{k} \cdot \mathbf{t}_B}, 0, e^{i\mathbf{k} \cdot \mathbf{t}_B})^T. \end{aligned} \quad (33)$$

With the above trial Wannier basis, we calculate (the logarithm of) the determinant of the overlap matrix $\det[\mathcal{S}(\mathbf{k})]$. As shown in Fig. 5 (a) and (b), we find that the determinant remains finite throughout the BZ, which confirms the absence of an obstruction in describing C_3 -symmetric $\text{FT}_{\#1}^{\odot}$ with our trial Wannier basis. In other words, when breaking C_6 down to C_3 , the $\text{FT}_{\#1}^{\odot}$ phase becomes trivialized and is adiabatically connected to an atomic insulator $s@q_{2b}$.

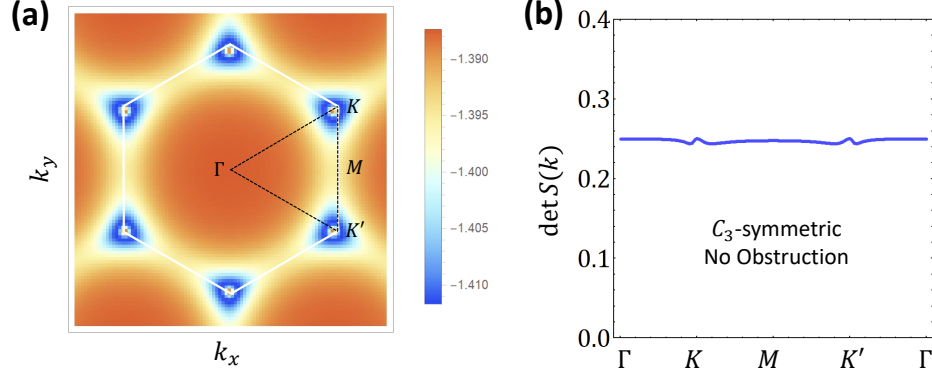


FIG. 5. $\log(\det[S(\mathbf{k})])$ of $\text{FT}_{\#1}^{\text{O}}$ in the presence of a C_6 -breaking staggered potential (a) for the entire BZ; (b) along the high symmetry lines.

Appendix C: Floquet π -flux model

Effective Floquet Hamiltonian from High Frequency Expansion

In this section, we derive the effective Floquet Hamiltonian (5) in the main text for the driven π -flux model using high frequency expansion. The time-dependent Hamiltonian of the π -flux model coupled to a vector potential $\mathcal{A}(\tau) = A(\cos\omega\tau, \sin\omega\tau)$ is given by:

$$H(\tau) = \sum_{\langle ij \rangle} t_{ij}(\tau) c_i^\dagger c_j + \text{H.c.} \quad (34)$$

$$\begin{aligned} t_{ij}(\tau) &= t_{ij} \exp \left(-i \int_{\mathbf{r}_i}^{\mathbf{r}_j} \mathcal{A}(\tau) \cdot d\mathbf{r} \right) \\ &= t_{ij} \exp \left[-i \mathcal{A}(\tau) \cdot (\mathbf{r}_j - \mathbf{r}_i) \right]. \end{aligned} \quad (35)$$

The Floquet Hamiltonian H_F is defined via the stroboscopic time evolution operator:

$$U_F = \mathcal{T} \exp \left(-i \int_0^T H(\tau) d\tau \right) \equiv \exp(-i H_F T), \quad (36)$$

where $T = \frac{2\pi}{\omega}$. To leading order in $1/\omega$, the effective Hamiltonian can be written as [40]:

$$H_F = H_0 + \sum_{m \neq 0} \frac{[H_{-m}, H_m]}{2m\omega} + \mathcal{O}(\omega^{-2}), \quad (37)$$

where

$$H_0 = \frac{1}{T} \int_0^T d\tau H(\tau), \quad H_m = \frac{1}{T} \int_0^T d\tau H(\tau) e^{-im\omega\tau} \quad (38)$$

are the Fourier components of $H(\tau)$. For Hamiltonian (34) with NN hopping, the only nonvanishing term in $[H_{-m}, H_m]$ gives rise to a second NN hopping. The Floquet Hamiltonian thus takes the following form:

$$H_F = \sum_{\langle ij \rangle} t_{1,ij} c_i^\dagger c_j + \sum_{\langle\langle ij \rangle\rangle} t_{2,ij} c_i^\dagger c_j + \text{H.c.} + \mathcal{O}(\omega^{-2}), \quad (39)$$

where $t_{1,ij}$ and $t_{2,ij}$ denotes NN and NNN hopping respectively, and

$$t_{1,ij} = \frac{1}{T} \int_0^T d\tau t_{ij}(\tau), \quad t_{2,ij} = \sum_{m \neq 0} \sum_k \frac{t_{ik}^{-m} t_{kj}^m}{m\omega}, \quad t_{ij}^m = \frac{1}{T} \int_0^T d\tau t_{ij}(\tau) e^{-im\omega\tau}. \quad (40)$$

The Fourier components of $t_{ij}(\tau)$ can be calculated explicitly. We first rewrite:

$$\begin{aligned} t_{ij}(\tau) &= t_{ij} \exp[-i\mathcal{A}(\tau) \cdot (\mathbf{r}_j - \mathbf{r}_i)] \\ &= t_{ij} \exp[-iA(\cos\omega\tau \cos\phi_{ij} + \sin\omega\tau \sin\phi_{ij})] \\ &= t_{ij} \exp[-iA\cos(\omega\tau - \phi_{ij})], \end{aligned} \quad (41)$$

where we have defined the bond angle ϕ_{ij} via $\mathbf{r}_{ij} \equiv \mathbf{r}_j - \mathbf{r}_i = (\cos\phi_{ij}, \sin\phi_{ij})$. Now we can compute the Fourier components:

$$\begin{aligned} t_{ij}^m &= \frac{1}{T} \int_0^T d\tau t_{ij} e^{-iA\cos(\omega\tau - \phi_{ij})} e^{-im\omega\tau} \\ &= \frac{1}{2\pi} \int_0^{2\pi} dx t_{ij} e^{-iA\sin x} e^{-imx} e^{-im\phi_{ij}} \\ &= t_{ij} \mathcal{J}_m(A) e^{-im\phi_{ij}}, \end{aligned} \quad (42)$$

where $\mathcal{J}_m(A)$ is the m -th Bessel function of the first kind. It is then straightforward to show $t_{1,ij} = t_{ij} \mathcal{J}_0(A)$ is the renormalized NN hopping, and

$$\begin{aligned} t_{2,ij} &= \sum_{m \neq 0} \sum_k \frac{t_{ik} t_{kj}}{m\omega} (-1)^m \mathcal{J}_m^2(A) e^{im(\phi_{ik} - \phi_{kj})} \\ &= i \sum_k \sum_{m=1}^{\infty} \frac{2t_{ik} t_{kj}}{m\omega} (-1)^m \mathcal{J}_m^2(A) \sin[m(\phi_{ik} - \phi_{kj})] \\ &= -i\eta_{ij} \sum_{m \text{ odd}, m>0} \frac{4it^2}{m\omega} \mathcal{J}_m^2(A) \sin\left(\frac{\pi}{2}m\right) \\ &= \frac{4\eta_{ij}t^2}{\omega} \sum_{m \text{ odd}, m>0} \frac{\mathcal{J}_m^2(A)}{m} \sin\left(\frac{\pi}{2}m\right) \end{aligned} \quad (43)$$

is the driving-induced NNN hopping, where $\eta_{ij} = \pm 1$ is a sign depending on the hopping direction as well as the even/odd column index of site i , as illustrated in Fig. 3(a) in the main text. It is easy to see that the flux through each triangle is $B_{\Delta} = \pm \frac{\pi}{2}$, thus the NNN hopping breaks time-reversal symmetry and gaps out the Dirac cones. We have thus derived the Floquet Hamiltonian (5) in the main text.

Edge Theory of H_{\square}

To construct the FT insulator, we couple two copies of π -flux models with opposite spins under oppositely polarized drives. The FT phases arise when the hoppings satisfy: $t_{1\uparrow}t_{1\downarrow} < 0$, $t_{2\uparrow}t_{2\downarrow} < 0$. Since the Chern number of the occupied bands in the two copies are $C = \pm 1$, we expect a pair of counter-propagating chiral edge modes at the boundary. However, as we will show in this section, these edge modes can be gapped out by the coupling H_g in the main text. We demonstrate this by constructing the low energy effective edge theory of H_{\square} .

At low energy, we start by linearizing H_{\square} around the two Dirac points in momentum space:

$$H = -v_F(p_x\sigma^x \otimes \mathbb{1} + p_y\sigma^z \otimes \tau^z) \otimes \gamma^z + m\sigma^y \otimes \tau^z \otimes \gamma^z, \quad (44)$$

where $v_F = 2t_1$, $m = 4t_2$, and Pauli matrices σ , τ and γ act on sublattice, valley and spin degrees of freedom respectively. We shall hereafter omit the \otimes . Consider an edge of the system whose normal and tangential unit vectors are $\mathbf{n} = (\cos\theta, \sin\theta)$, $\mathbf{t} = (-\sin\theta, \cos\theta)$. Define $\Sigma \equiv (\sigma^x\gamma^z, \sigma^z\tau^z\gamma^z)$, and the effective Hamiltonian near the edge can be written as:

$$H_{\text{edge}} = iv_F \mathbf{n} \cdot \Sigma \partial_{\lambda} - v_F p_t \mathbf{t} \cdot \Sigma + m(\lambda) \sigma^y \tau^z \gamma^z, \quad (45)$$

where we have decomposed the momentum along the directions of \mathbf{n} and \mathbf{t} : $\mathbf{p} = p_n \mathbf{n} + p_t \mathbf{t}$, and further made the substitution $p_n \rightarrow -i\partial_{\lambda}$. The edge is modeled by a mass domain wall $m(\lambda)$ interpolating between $\pm m$ as $\lambda \rightarrow \pm\infty$. The edge modes are eigenstates of Hamiltonian (45) that are exponentially localized near the edge. We take the following ansatz wavefunction for the edge state:

$$\Psi \sim e^{-\frac{1}{v_F} \int_0^{\lambda} |m(\lambda')| d\lambda'} \psi(p_t), \quad (46)$$

up to normalization. Here we shall take $m(\lambda') > 0$ in the integrand for definiteness. Using this ansatz, we have

$$H_{\text{edge}}\Psi = [-v_F p_t \mathbf{t} \cdot \mathbf{\Sigma} + m(\lambda)\sigma^y \tau^z \gamma^z (1 - i\sigma^y \tau^z \gamma^z \mathbf{n} \cdot \mathbf{\Sigma})] \Psi. \quad (47)$$

If the second term in the above equation vanishes, we have the eigenvalue equation

$$-v_F p_t \mathbf{t} \cdot \mathbf{\Sigma} \psi(p_t) = E \psi(p_t). \quad (48)$$

To make the second term vanish, we simply require that $\psi(p_t)$ is an eigenstate of the projector:

$$\begin{aligned} P &\equiv \frac{1}{2} (1 + i\sigma^y \tau^z \gamma^z \mathbf{n} \cdot \mathbf{\Sigma}) \\ &= \frac{1}{2} (1 + \gamma^z \mathbf{t} \cdot \mathbf{\Sigma}), \end{aligned} \quad (49)$$

with $P\psi(p_t) = \psi(p_t)$. Apparently, the projector P and $-v_F p_t \mathbf{t} \cdot \mathbf{\Sigma}$ share the common set of eigenstates $\psi(p_t)$. Requiring $\gamma^z \mathbf{t} \cdot \mathbf{\Sigma} = 1$ yields the 2×2 projected edge Hamiltonian:

$$H_{\text{edge}}^P = -v_F p_t \gamma^z. \quad (50)$$

The two counter-propagating chiral edge modes have energies $E = -v_F p_t$ for $\gamma^z = 1$ (spin-up), and $E = v_F p_t$ for $\gamma^z = -1$ (spin-down), which are gapless.

Now we demonstrate that the pair of chiral edge modes can be gapped out with H_g in the main text. In momentum space, H_g reads:

$$\begin{aligned} H_g &= \sum_{\mathbf{k}} g_1 c_{o\mathbf{k},\uparrow}^\dagger c_{o\mathbf{k},\downarrow} - g_1 c_{e\mathbf{k},\uparrow}^\dagger c_{e\mathbf{k},\downarrow} + \text{H.c.} \\ &+ g_2 e^{-ik_x} c_{o\mathbf{k},\uparrow}^\dagger c_{e\mathbf{k},\downarrow} - g_2 e^{-ik_x} c_{o\mathbf{k},\downarrow}^\dagger c_{e\mathbf{k},\uparrow} + \text{H.c.}, \end{aligned} \quad (51)$$

where the subscript e/o labels sublattices in even and odd columns respectively. Near the Dirac points, H_g reduces to:

$$H_g = g_1 \sigma^z \gamma^x + g_2 \sigma^x \gamma^y. \quad (52)$$

We can now project H_g to the subspace of the edge states, making use of the fact $\gamma^z \mathbf{t} \cdot \mathbf{\Sigma} = 1$:

$$P H_g P = g_1 \cos \theta \tau^z \gamma^x - g_2 \sin \theta \gamma^y. \quad (53)$$

Since both mass terms anticommute with H_{edge}^P , we find that indeed they gap out the chiral edge modes. Notice that if only one of the two mass terms is present, either the x or the y edge will remain gapless (i.e. $\theta = 0$ or $\theta = \frac{\pi}{2}$), which we also verify numerically.

Appendix D: Fragile Topology of the Floquet π -flux model

Nontrivial Winding of the Wilson Loop

In this section, we show that the fragile topology in the Floquet π -flux model can be diagnosed from the Wilson loop. We take the $FT_{\#1}^\square$ phase in Fig. 3(b) of the main text as a concrete example. We compute the Wilson loop oriented along the k_y direction:

$$\begin{aligned} W_y^{mn}(k_x) &= \langle u^m(k_x, k_y + 2\pi) | u^r(k_x, k_y + 2\pi - \Delta k) \rangle \cdots \langle u^l(k_x, k_y + \Delta k) | u^n(k_x, k_y) \rangle \\ &\equiv \langle u^m(k_x, k_y + 2\pi) | \prod_{\mathbf{k}}^{k_y + 2\pi \leftarrow k_y} P(\mathbf{k}) | u^n(k_x, k_y) \rangle, \end{aligned} \quad (54)$$

where $P(\mathbf{k})$ is a projector onto the occupied bands. The set of eigenvalues of W_y is denoted as $\{e^{i2\pi\nu_y(k_x)}\}$, where $\{\nu_y(k_x)\}$ are the y coordinates of the Wannier centers of the occupied bands at k_x . In Fig. 6(a), we plot the Wannier centers as a function of k_x . We find that the Wilson loop exhibits a nontrivial winding across the BZ, indicating an obstruction towards a Wannier representation for the occupied bands of H_\square in the $FT_{\#1}^\square$ phase.

In fact, the winding of the Wilson loop in Fig. 6(a) is protected by the C_2 symmetry of H_\square . By inspecting the symmetry data in Fig. 3(b) of the main text, we find that the C_2 eigenvalues $\Gamma(-i, -i)$ and $Y(-i, -i)$ constrain the Wannier center $\nu_y(k_x = 0) = 0$, and the eigenvalues $X(-i, -i)$ and $M(i, i)$ constrain $\nu_y(k_x = \pm \frac{\pi}{2}) = \pm \frac{1}{2}$. Therefore, for H_\square with two occupied bands, the Wilson loop winding is robust as long as C_2 symmetry is preserved.

Addition of Atomic Orbitals

We now show that the nontrivial winding of the Wilson loop can be removed upon adding to H_\square atomic orbitals in a C_2 symmetric manner. As depicted by orange dots in Fig. 7, we add atomic orbitals with spin-up electrons at C_2 symmetric positions $(0, \pm 1/4)$ away from the original sites. We now couple the additional orbitals to the original model and arrive at the new Hamiltonian:

$$H = \begin{pmatrix} H_\square & H_c \\ H_c^\dagger & H_{\text{atom}} \end{pmatrix}, \quad (55)$$

where

$$H_{\text{atom}} = \begin{pmatrix} -\mu & re^{-i(k_x + \frac{k_y}{2})} \\ re^{i(k_x + \frac{k_y}{2})} & -\mu \end{pmatrix}, \quad (56)$$

and

$$H_c = \begin{pmatrix} ve^{-i\frac{k_y}{4}} & 0 \\ 0 & ve^{i\frac{k_y}{4}} \\ ve^{-i\frac{k_y}{4}} & 0 \\ 0 & -ve^{i\frac{k_y}{4}} \end{pmatrix}. \quad (57)$$

We have chosen the above form of H_{atom} and H_c such that the C_2 symmetry is preserved.

In Fig. 6(b), we compute the Wilson loop of the occupied bands of the new Hamiltonian (55). We find that the Wilson loop unwinds upon adding trivial atomic orbitals, indicating that the composite system is Wannierizable.

Atomic Decomposition

To further demonstrate that the phases $\text{FT}_{\#1}^\square$ and $\text{FT}_{\#2}^\square$ of H_\square are indeed Wannier obstructed, we construct explicitly their decompositions in terms of atomic orbitals.

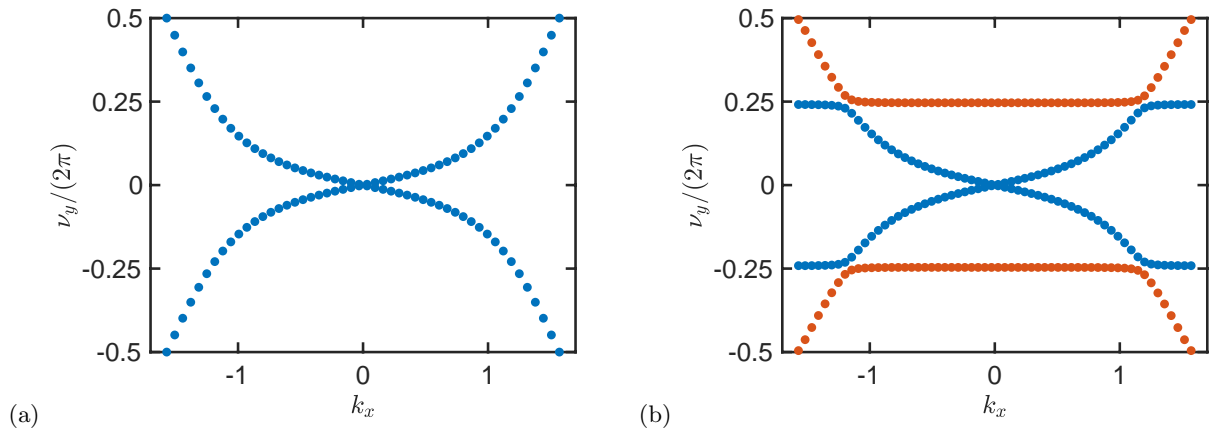


FIG. 6. (a) Wannier centers of the occupied bands of H_\square in phase $\text{FT}_{\#1}^\square$ as a function of k_x . The eigenvalues at $k_x = 0$ and $\pm \frac{\pi}{2}$ are protected by the C_2 eigenvalues at the high symmetry points of the Brillouin zone. (b) The Wilson loop unwinds upon adding two atomic orbitals at $(0, 1/4)$ and $(0, -1/4)$ to H_\square . We choose parameters $t_{1\uparrow} = -t_{1\downarrow} = 1$, $t_{2\uparrow} = -t_{2\downarrow} = 0.6$, $g_1 = 0.3$, $g_2 = 0.4$, $\mu = 10$, $r = 0.5$, and $v = 1.5$.

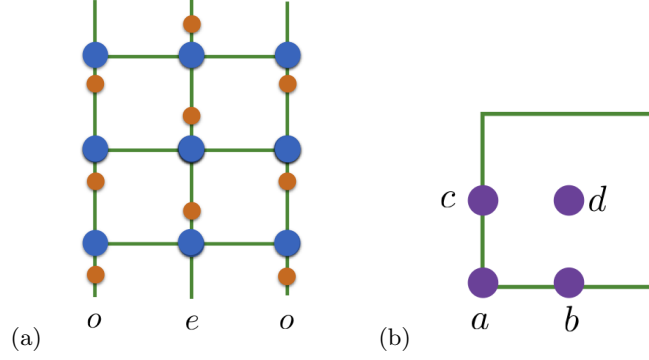


FIG. 7. (a) Lattice with additional atomic orbitals depicted as orange dots. These orbitals are added in C_2 related pairs at positions $(0, \pm 1/4)$ away from the original lattice sites. (b) Four maximal Wyckoff positions of the square lattice.

	$s_{\uparrow}@q_{1a}$	$s_{\uparrow}@q_{1b}$	$s_{\uparrow}@q_{1c}$	$s_{\uparrow}@q_{1d}$	$s_{\downarrow}@q_{1a}$	$s_{\downarrow}@q_{1b}$	$s_{\downarrow}@q_{1c}$	$s_{\downarrow}@q_{1d}$
Γ	$-i$	$-i$	$-i$	$-i$	i	i	i	i
X	$-i$	i	$-i$	i	i	$-i$	i	$-i$
Y	$-i$	$-i$	i	i	i	i	$-i$	$-i$
M	$-i$	i	i	$-i$	i	$-i$	$-i$	i

TABLE II. C_2 eigenvalues at high symmetry momenta obtained by putting atomic orbitals at four maximal Wyckoff positions. We only consider s orbitals with two spin species.

In Table II, we list the C_2 eigenvalues at high symmetry momenta obtained from putting atomic orbitals at four maximal Wyckoff positions of the square lattice [Fig. 7(b)]. We consider only s orbitals with two spin species. Comparing with Fig. 3(b) in the main text, we find that the fragile topological phases of H_{\square} can be decomposed as follows:

$$\text{FT}_{\#1}^{\square} = (s_{\uparrow}@q_{1a}) \oplus (s_{\uparrow}@q_{1b}) \oplus (s_{\uparrow}@q_{1c}) \ominus (s_{\uparrow}@q_{1d}), \quad (58)$$

$$\text{FT}_{\#2}^{\square} = (s_{\downarrow}@q_{1a}) \oplus (s_{\downarrow}@q_{1b}) \oplus (s_{\downarrow}@q_{1d}) \ominus (s_{\downarrow}@q_{1c}). \quad (59)$$

Indeed, both $\text{FT}_{\#1}^{\square}$ and $\text{FT}_{\#2}^{\square}$ can be represented as subtracting an atomic insulator from another atomic insulator, which indicates that both phases exhibit fragile topology.

Upon adding atomic orbitals and forming the composite Hamiltonian (55), the system becomes Wannierizable and hence should be representable in terms of atomic orbitals. We take $\text{FT}_{\#1}^{\square}$ as an example. The symmetry data for Hamiltonian (55) by coupling with $\text{FT}_{\#1}^{\square}$ are: Γ $(-i, -i, i, -i)$, X $(-i, -i, i, -i)$, Y $(-i, -i, i, -i)$, and M $(i, i, i, -i)$. By inspecting Table II, we find that the composite system can be represented as $(s_{\uparrow}@q_{1a}) \oplus (s_{\uparrow}@q_{1b}) \oplus (s_{\uparrow}@q_{1c}) \oplus (s_{\downarrow}@q_{1d})$, which is indeed an atomic insulator.

Mirror-protected Fragile Topology of the Floquet π -flux Model

Along the mirror-symmetric line in Fig. 3(c) of the main text, the system further preserves mirror symmetries M_x and M_y . In this case, atomic decompositions must also take into account mirror symmetry representations, which leads to new mirror-protected fragile phases, mirror- $\text{FT}_{\#1}^{\square}$ and mirror- $\text{FT}_{\#2}^{\square}$. Since $[M_x, M_y] = 0$, the symmetry data consist of (m_x, m_y) at each high symmetry momenta, which is a pair of simultaneous eigenvalues of M_x and M_y . We list the symmetry data for our target fragile phases and possible atomic insulators in Table. III. For the atomic phases in Table. III, we have only listed cases with an atomic orbital carrying $m_x = +i$, while the situation with $m_x = -i$ can be derived similarly by simply flipping the sign of m_x .

By comparing with the atomic data, we again find that no two-band atomic insulator could match the symmetry data for either mirror- $\text{FT}_{\#1}^{\square}$ or mirror- $\text{FT}_{\#2}^{\square}$, which implies the existence of Wannier obstruction. On the other hand, we find that the two phases yield the following atomic decompositions:

$$\begin{aligned} \text{mirror-FT}_{\#1} &\equiv (-, -)@q_{1a} \oplus (+, +)@q_{1b} \oplus (+, +)@q_{1c} \ominus (+, +)@q_{1d}, \\ \text{mirror-FT}_{\#2} &\equiv (-, +)@q_{1a} \oplus (+, -)@q_{1b} \oplus (+, +)@q_{1c} \ominus (+, +)@q_{1d}, \end{aligned} \quad (60)$$

System	mirror-FT _{#1}	mirror-FT _{#2}	(+,+)@1a	(+,+)@1b	(+,+)@1c	(+,+)@1d	(+,-)@1a	(+,-)@1b	(+,-)@1c	(+,-)@1d
Γ	(+,+) (-,-)	(+, -) (-, +)	(+, +)	(+, +)	(+, +)	(+, +)	(+, -)	(+, -)	(+, -)	(+, -)
X	(+,+) (-,-)	(+,+) (-, -)	(+, +)	(-, +)	(+, +)	(-, +)	(+, -)	(-, -)	(+, -)	(-, -)
Y	(+,+) (-,-)	(+, -) (-, +)	(+, +)	(+, +)	(+, -)	(+, -)	(+, -)	(+, -)	(+, +)	(+, +)
M	(+, -) (-, +)	(+, -) (-, +)	(+, +)	(-, +)	(+, -)	(-, -)	(+, -)	(-, -)	(+, +)	(-, +)

TABLE III. Mirror eigenvalues (m_x, m_y) at high symmetry momenta for mirror-FT_{#1} and mirror-FT_{#2} and various atomic insulators. Here we denote $(\pm i, \pm i) = (\pm, \pm)$ for short.

which indicates mirror-protected fragile topology.